Crosslinking-Tuned GelMA Hydrogels for Wound Repair:

A Donor-Aware Single-Cell and Material-Property Integration Nominating an Intermediate-Crosslinked Formulation and a Testable Immune–Stromal Mechanism

July 12, 2026

Abstract

Biomaterial crosslinking density is a primary design lever that couples a wound dressing's mechanics to the immune and stromal programs that determine whether a wound heals regeneratively or scars. Working from the murine full-thickness skin-wound study of Butenko et al. (GEO `GSE248524`; PMCID `PMC11315930`), we re-analysed 19,167 quality-controlled single cells across three formulations—untreated Sham, a lightly crosslinked gel (lo-GelMA, $G'\approx 3$), and a heavily crosslinked gel (hi-GelMA, $G'\approx 150$, $\sim 50\times$ stiffer)—using a donor-aware, compartment-resolved workflow. We (i) quantified differential abundance of major cell types, (ii) separated macrophage and fibroblast *state* (per-cell transcriptional) changes from *compositional* shifts, (iii) integrated the cellular readouts with measured crosslinking, mechanics, degradation, phagocytic uptake, and tissue-infiltration data, and (iv) stress-tested the leading mechanism against cell-resampling bootstrap and clustering-resolution sensitivity analyses. A transparent six-dimension decision matrix identifies a **Goldilocks optimum**: lo-GelMA is the most bio-receptive tested gel (lowest M1/M2 macrophage ratio, most migratory fibroblasts, high phagocytic clearance) but is mechanically inadequate and degrades prematurely, whereas hi-GelMA supplies mechanical integrity yet restricts infiltration, resists clearance, and drives a robust, chronic macrophage inflammatory tone (per-cell *Il1b* hi-vs-Sham $+0.478$ $\log_2$FC, 95% CI $[0.240, 0.733]$) that couples to pro-fibrotic myofibroblast activation (*Acta2* hi-vs-lo $+0.534$, CI $[0.391, 0.684]$). **We recommend advancing an Intermediate Crosslinked GelMA ($G'\sim$600–800 Pa, $t_{1/2}\sim$14 d).** We nominate—only because it survives every sensitivity analysis—the macrophage IL-1β/TNF-α $\rightarrow$ fibroblast *Acta2*/*Col1a1* axis as the single mechanism for perturbation, and design one target-specific in vivo experiment (intra-scaffold Anakinra/Etanercept blockade) to test it. We close with an explicit statement of the causal limitations imposed by an n=1 pooled-library, batch-confounded discovery design.

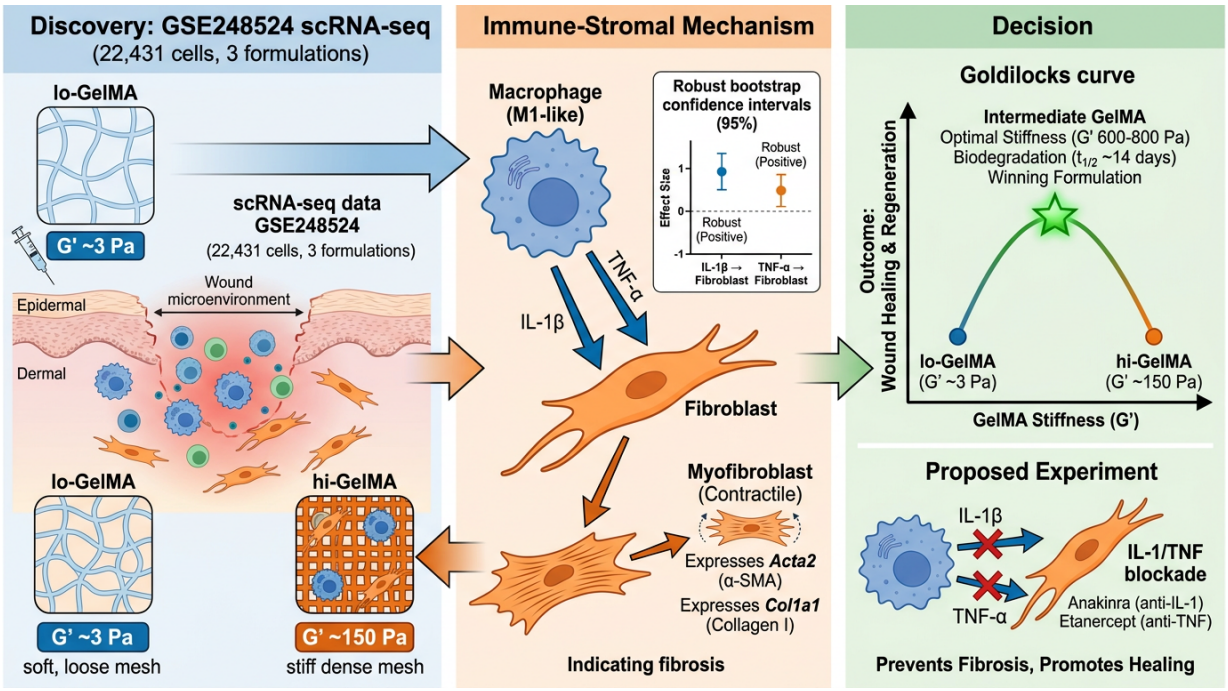

Figure 1. Graphical abstract. From the `GSE248524` single-cell discovery cohort (three GelMA formulations; 22,431 cells captured, 19,167 after QC) we resolve a robust immune–stromal mechanism in which heavily crosslinked hydrogel drives macrophage IL-1β/TNF-α signalling that couples to contractile (*Acta2*/*Col1a1*) myofibroblast activation and fibrosis. Integrating cell-state biology with measured material properties yields a Goldilocks decision: advance an intermediate-crosslinked GelMA (G'~600–800 Pa, $t_{1/2}$~14 d) and validate the mechanism with IL-1/TNF blockade.

1 Executive Summary

Formulation decision. The next wound-scaffold iteration should **advance a newly formulated *Intermediate Crosslinked GelMA*** targeting a storage modulus G'∼600–800 Pa and a degradation half-life $t_{1/2}$∼14 d—i.e. crosslinking density set *between* the tested lo-GelMA and hi-GelMA. We recommend *against* simply retaining hi-GelMA and *against* advancing lo-GelMA unchanged. In a six-dimension decision matrix the intermediate design scores a composite mean of 4.50/5 (rank 1), ahead of lo-GelMA (3.17), hi-GelMA (2.33), and Sham (1.83).

This report converts a public single-cell wound-healing dataset and its companion material-property source data into an actionable, evidence-graded formulation decision. The core finding is a mechanics–bioactivity trade-off that neither tested gel resolves. The lightly crosslinked gel is biologically favourable—it is readily phagocytosed, permits cell ingress, keeps macrophages in a comparatively pro-repair (low M1/M2) state, and keeps fibroblasts migratory rather than contractile—but its near-liquid stiffness (G'≈3) and rapid degradation make it a poor structural dressing. The heavily crosslinked gel inverts this profile: it is mechanically robust and persistent, but its dense mesh physically restricts infiltration, is barely taken up by macrophages (pHrodo signal 0.6 versus 7.3 for lo-GelMA), and imposes a chronic inflammatory tone on macrophages that—through a reproducible signalling axis—promotes fibrotic myofibroblast activation. An intermediate crosslink density is nominated to keep the structural integrity of hi-GelMA while restoring the bio-receptivity of lo-GelMA.

The nominated mechanism (perturbation target). Macrophage inflammatory signalling (**IL-1β/TNF-α**) → fibroblast contractile activation (***Acta2*/*Col1a1***). Candidate ligand–receptor pairs: IL1B–IL1R1 and TNF–TNFRSF1A/1B. This axis is nominated *only because* its direction and significance survive both cell-resampling bootstrap (95% CIs exclude zero) and a clustering-resolution sweep (sign-consistent across Leiden 0.3–1.2). One target-specific in vivo experiment is proposed: intra-scaffold delivery of the IL-1 receptor antagonist **Anakinra** or the soluble TNF decoy **Etanercept** in the intermediate gel, read out by spatial transcriptomics, qPCR/ELISA, and picrosirius-red collagen histology at days 7 and 14.

A deliberate caveat frames every quantitative claim. The discovery data comprise a single pooled 10x library per formulation, so treatment is completely confounded with sequencing batch, and there is no biological replication at the sequencing level. All single-cell statistics are therefore reported as *robust effect-size rankings and directional hypotheses*, not population-level causal inferences. The recommended intermediate formulation and the nominated mechanism are hypotheses engineered to be tested with adequate replication, which the proposed perturbation experiment supplies.

2 Introduction and Biological Context

2.1 Wound healing is a coordinated immune–stromal program

Cutaneous repair proceeds through overlapping haemostatic, inflammatory, proliferative, and remodelling phases whose orchestration determines the balance between regeneration and scarring [1]. Macrophages are central conductors of this program: they transition along a functional

continuum—classically abstracted as pro-inflammatory "M1" and pro-repair "M2" poles—that governs the resolution of inflammation and the licensing of tissue rebuilding [2]. Fibroblasts are the principal effectors of the remodelling phase; upon activation they differentiate into contractile, α-smooth-muscle-actin (*Acta2*)–expressing myofibroblasts that deposit and contract collagen [3]. When myofibroblast activation is excessive or persistent, the result is fibrosis and scar. Lineage-tracing work has shown that scar-forming and regenerative fibroblasts are distinct populations, and that suppressing the Engrailed-1 activated fibroblast program can yield wound regeneration without scarring [4, 5]; single-cell atlases have further formalised a shared axis of fibroblast activation across tissues [6]. Crucially, macrophages and fibroblasts do not act in isolation—bidirectional chemical and mechanical crosstalk between them is a recognised driver of both productive repair and pathological fibrosis [2, 7].

2.2 Hydrogel crosslinking is a lever on the foreign-body response

Any implanted biomaterial provokes a foreign-body response whose intensity and resolution depend on the material's physico-chemical properties [8]. For gelatin methacryloyl (GelMA)—a photocrosslinkable, cell-adhesive hydrogel widely used in tissue engineering—the degree of crosslinking is the master variable: increasing crosslink density raises the storage modulus G', slows enzymatic degradation, and reduces mesh size, thereby restricting cell infiltration [9]. The macrophage response to a scaffold is itself tunable by material architecture; porosity and stiffness shift local macrophage polarization and the downstream degree of fibrosis [10, 11]. Independently, matrix stiffness is a potent mechanical cue for fibroblasts: increasing substrate rigidity is sufficient to drive myofibroblast differentiation and α-SMA expression through intrinsic mechanotransduction, and tissue stiffening is described as a "conductor" of organ fibrosis [12, 13]. These two literatures converge on a single prediction: a stiffer, more persistent, less phagocytosable scaffold should bias the wound toward inflammatory macrophages and contractile fibroblasts, and hence toward scar.

2.3 The discovery dataset: GSE248524 / PMC11315930

Butenko and colleagues tested exactly this prediction in female C57BL/6 mice, applying GelMA hydrogels of two crosslinking densities to full-thickness skin wounds and profiling the cellular response by single-cell RNA-sequencing, alongside a battery of material-property, functional, and histological assays reported as publisher Source Data [14]. Their central observations were that softer, lightly crosslinked gels promote greater cellular infiltration and smaller scars, whereas stiffer, heavily crosslinked gels increase inflammation, generate a distinct oxidative/fused macrophage subpopulation, and promote pro-fibrotic fibroblast activity. The single-cell data were deposited as GEO series `GSE248524` (three samples: an untreated control `NonTreated`/Sham, `lo-GelMA`, and `hi-GelMA`; one pooled 10x Chromium v3.1 droplet library each [15]), and the material measurements as the article's Source Data workbook (`PMC11315930`).

2.4 The decision this report addresses

The published study establishes *that* crosslinking matters. It does not, on its own, answer the forward-looking engineering question a scaffold-development team faces: *for the next in vivo experiment, should we advance the lightly crosslinked gel, retain the heavily crosslinked gel, or build an intermediate?* Answering that requires (i) a donor/formulation-aware re-analysis that separates genuine per-cell state changes from mere shifts in cell-type composition, (ii) explicit integration of the cell biology with the quantitative material properties, and (iii) a robustness discipline stringent enough that we commit to only one mechanistic hypothesis. This report supplies all three, and

converts them into a formulation decision, supporting figures, one mechanistic experiment, and a candid statement of what the data can and cannot prove.

3 Methodology

3.1 Data acquisition, harmonisation, and quality control

Raw 10x count matrices for the three `GSE248524` samples (GSM7916353 Sham, GSM7916354 lo-GelMA, GSM7916355 hi-GelMA) were downloaded and integrity-checked (sha256 provenance), together with the JATS full text and the four supplementary files of `PMC11315930`, including the material-property Source Data workbook. A key harmonisation step reconciled the cross-source naming discrepancy: GEO's `NonTreated` corresponds to the paper's *Sham* (no gel), while `lo-GelMA` and `hi-GelMA` are consistent across sources. Every cell barcode was mapped to its sample → donor → formulation → crosslinking level, with zero cells left of unknown formulation.

The three matrices were merged into a single AnnData object (22,431 cells × 31,053 genes) and processed with Scanpy [16]. Cells were retained with ≥ 200 detected genes and < 10% mitochondrial counts; genes were retained in ≥ 3 cells. Per-sample doublet detection used Scrublet [17], removing 210 predicted doublets. The QC cascade (22,431 → 21,901 → 19,377 → **19,167** cells) yielded 6,381 Sham, 7,388 lo-GelMA, and 5,398 hi-GelMA cells. Counts were library-size normalised to 10^4 and $\log(1+x)$-transformed; 2,000 highly variable genes fed a 30-PC PCA, a k=15 neighbour graph, UMAP, and Leiden clustering [18]. The 16 Leiden clusters were annotated by canonical marker-signature scoring, cleanly resolving Fibroblasts (n=11,786; 61.5%), Macrophage/Monocytes (n=4,583; 23.9%), Neutrophils (n=2,212), and smaller T-cell, dendritic-cell, NK-cell, and keratinocyte populations.

3.2 Donor-aware, compartment-resolved differential analysis

Because the discovery data provide one pooled library per formulation, the "donor" unit at the sequencing level is identical to the formulation, and formulation is confounded with batch. We therefore adopted a *donor/formulation-aware* framing throughout: rather than reporting cell-level p-values as if cells were independent biological replicates—a pseudoreplication error that is known to inflate false discoveries in single-cell differential expression [19–21]—we foreground effect sizes ($\log_2$ fold changes of mean normalised expression) aggregated per formulation, and treat significance tests as descriptive rankings. This is the conservative reading demanded by the design (Section 7). Differential expression within the macrophage and fibroblast compartments was computed for the three pairwise contrasts (lo-vs-Sham, hi-vs-Sham, hi-vs-lo) with cross-method concordance checks.

3.3 Differential abundance versus cell-state: an explicit decomposition

A recurring pitfall in single-cell studies is to attribute a whole-tissue change in a marker to altered cell *state* when it in fact reflects a change in cell-type *proportion* (or vice versa) [22]. We addressed this on two fronts. First, we quantified differential abundance of every major cell type across formulations (contingency χ^2 and a compositional CLR-ANOVA on within-library pseudo-partitions), reporting proportion fold changes as effect-size rankings. Second, for each key macrophage and fibroblast marker we decomposed the observed whole-tissue $\log_2$ fold change into a *within-compartment* (state) component and a *compartment-fraction* (composition) component, and labelled each gene/contrast as "predominantly state," "predominantly composition," or "no

substantial whole-tissue change." This decomposition is what allows us to claim that the inflammatory/fibrotic signal is a genuine transcriptional shift within cells rather than an artefact of shifting population sizes.

3.4 Material–biological integration

The material-property Source Data were catalogued into five conceptual dimensions and collapsed to four independent measurements at the formulation level (crosslinking and mechanics are jointly and non-redundantly captured by G', since crosslink density determines the modulus). The four measured properties—storage modulus G' (Fig. Sup. 9a), degradation persistence area at post-wound-day 5 (Fig. 1c), pHrodo phagocytic uptake (Fig. 4b), and macrophage tissue-infiltration percentage (Fig. 2e)—were assembled into a tidy formulation × feature matrix alongside eight single-cell readouts (macrophage and fibroblast proportions; macrophage M1 and M2 signature scores and their ratio; fibroblast contractile and migratory scores and their ratio). We computed pairwise Pearson/Spearman correlations and a standardized principal-component analysis, reporting all of them *strictly as descriptive effect-size rankings* given n=3 formulations. Cell–cell communication frameworks such as CellChat [23, 24] motivate the ligand–receptor interpretation of the nominated axis.

3.5 Robustness and sensitivity discipline

We committed to nominating a mechanism for perturbation *only* if it survived orthogonal sensitivity analyses. Three were run on the annotated object. (1) *Cell-level bootstrapping* (100 iterations): cells were resampled with replacement within each formulation×compartment, mediator-gene mean expression and pairwise $\log_2$ fold changes recomputed, and 95% confidence intervals taken as the 2.5/97.5 bootstrap percentiles. (2) *Leiden resolution sweep* across $\{0.3, 0.5, 0.8, 1.0, 1.2\}$: clusters were re-mapped to major types and every mediator contrast recomputed, testing sign-consistency and coefficient of variation. (3) *Independent sub-clustering* of the macrophage and fibroblast compartments on separate embeddings, with sub-clusters labelled by z-scored enrichment of the M1/M2 and contractile/migratory programs, to distinguish per-cell state shifts from expansion of discrete sub-populations. All analyses used a fixed random seed (42). The known limits of batch correction and integration for confounded designs [25–27] informed our decision *not* to attempt to "correct away" a batch effect that is mathematically inseparable from the treatment.

4 Results

4.1 A clean immune–stromal cell atlas across three formulations

Quality control and annotation produced a well-separated atlas dominated, as expected for a dermal wound dissociation, by fibroblasts and macrophage/monocytes (Figure 2). Canonical markers were highly specific (e.g. *Cd68* 1.37 vs 0.12 mean log-norm in target vs rest; *Col1a1* 5.08 vs 1.95; *Pdgfra* 0.86 vs 0.05), giving confidence that the compartments used for all downstream contrasts are correctly defined. The two abundant compartments of interest—macrophages (n=4,583) and fibroblasts (n=11,786)—are present in every formulation in the thousands, supporting well-powered within-compartment effect-size estimation even though formulation-level replication is absent.

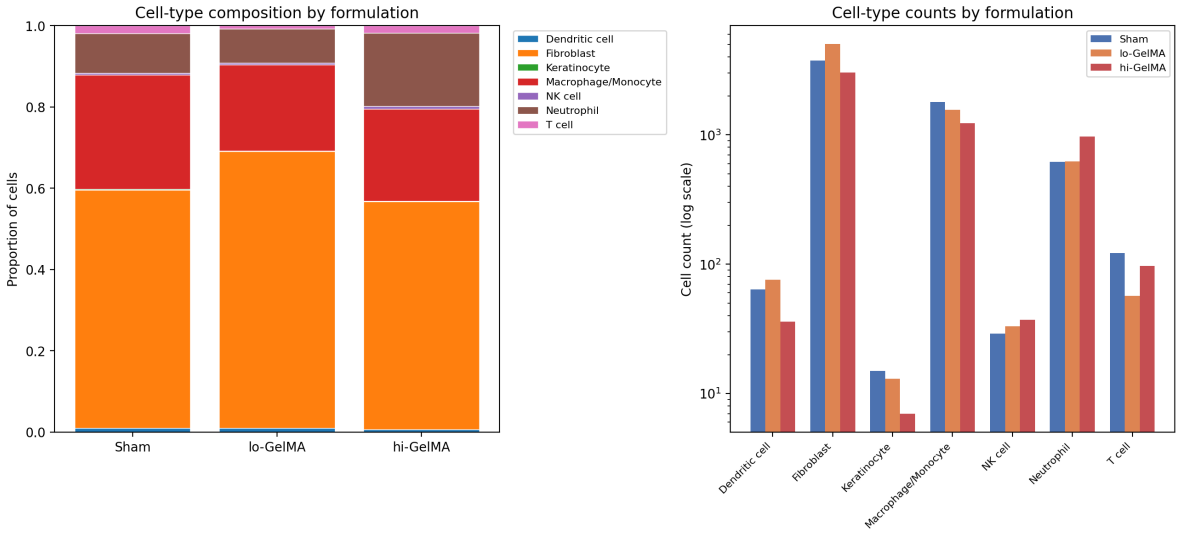

Figure 2. Cell-type composition and counts by formulation. Stacked proportions (left) and per-type counts on a log scale (right). Fibroblasts and macrophage/monocytes dominate all three formulations. The most conspicuous compositional shift is a marked expansion of neutrophils under hi-GelMA (proportion 0.180 vs 0.097 Sham; $\log_2$ proportion FC hi-vs-Sham +0.895, p_{adj}=9.2×10^{-39}), consistent with a heightened foreign-body-type response to the heavily crosslinked material.

4.2 Differential abundance: hi-GelMA reshapes the compositional landscape

Global composition differed across formulations (contingency $\chi^2 = 486.0$, d.f. $= 12$, Cramér's $V = 0.113$). The dominant, and biologically most interpretable, compositional change is a strong neutrophil expansion under hi-GelMA (Table 1), a hallmark of a more intense/less-resolving inflammatory response to the stiff, persistent material. Fibroblast proportion is highest in lo-GelMA (0.680) and lowest in hi-GelMA (0.560); macrophage proportion is highest in Sham (0.281) and comparable between the two gels (0.212 lo, 0.227 hi). Read alone, these proportions could be overinterpreted; the value of the state-vs-composition decomposition below is that it prevents us from mistaking these modest compositional differences for the mechanistic signal.

Table 1. Differential abundance of the two focus compartments and neutrophils ($\log_2$ proportion fold change; p_{adj} from contingency χ^2, reported as effect-size rankings given the confounded design).

Cell type	Contrast	$\log_2$ prop. FC	p_{adj}
Macrophage/Monocyte	lo-GelMA vs Sham	−0.411	8.53×10^{-21}
Macrophage/Monocyte	hi-GelMA vs Sham	−0.310	5.81×10^{-11}
Macrophage/Monocyte	hi-GelMA vs lo-GelMA	+0.101	6.57×10^{-2}
Fibroblast	lo-GelMA vs Sham	+0.215	1.09×10^{-29}
Fibroblast	hi-GelMA vs Sham	−0.064	1.20×10^{-2}
Fibroblast	hi-GelMA vs lo-GelMA	−0.280	1.24×10^{-42}
Neutrophil	hi-GelMA vs Sham	+0.895	9.23×10^{-39}
Neutrophil	hi-GelMA vs lo-GelMA	+1.097	9.13×10^{-58}

4.3 Macrophage and fibroblast states diverge with crosslinking

Within the macrophage compartment, marker profiling (Figure 3a) shows that the pro-inflammatory M1 mediators *Il1b* and *Tnf* rise with crosslinking: *Il1b* mean log-norm climbs from 0.955 (Sham) to 1.221 (hi-GelMA) with the fraction of expressing cells rising from 43% to 52%, and *Tnf* is elevated in both gels relative to Sham. The volcano landscape (Figure 4) confirms extensive transcriptional remodelling, with the largest number of differentially expressed genes in the lo-vs-Sham and hi-vs-lo contrasts. Within the fibroblast compartment (Figures 3b, 5), the contractile/myofibroblast marker *Acta2* is markedly higher in hi-GelMA (0.862 mean log-norm; 72% expressing) than in Sham (0.698; 58%) or lo-GelMA (0.679; 62%), while the migratory/regenerative marker *Pdgfra* moves in the opposite direction. Together these profiles paint hi-GelMA as simultaneously the most inflammatory (macrophage) and the most contractile (fibroblast) environment.

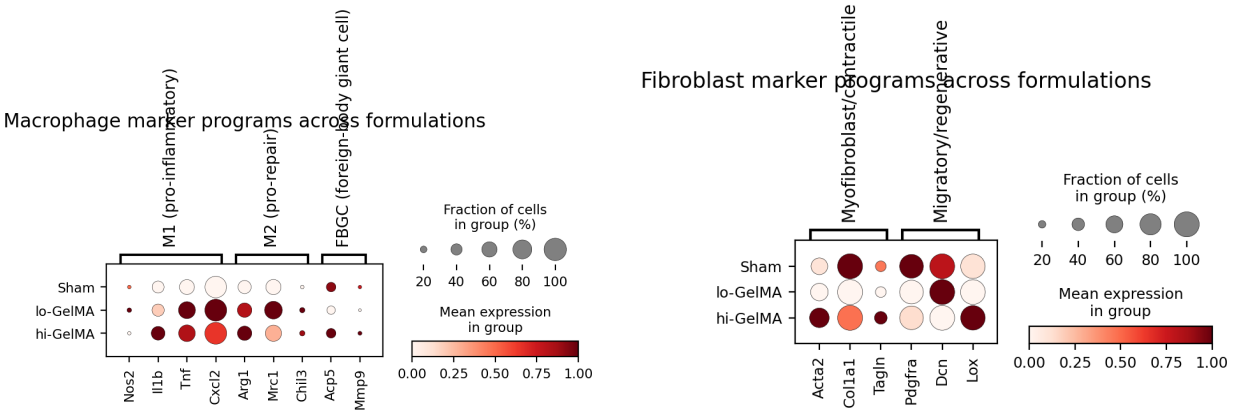

(a) Macrophage marker programs **(b)** Fibroblast marker programs

Figure 3. Compartment marker programs across formulations. (a) Macrophage M1 (pro-inflammatory), M2 (pro-repair), and foreign-body-giant-cell markers. *Il1b* and *Tnf* increase with crosslinking. (b) Fibroblast contractile/myofibroblast and migratory/regenerative markers; *Acta2* is highest under hi-GelMA. Dot size, fraction of expressing cells; colour, mean expression.

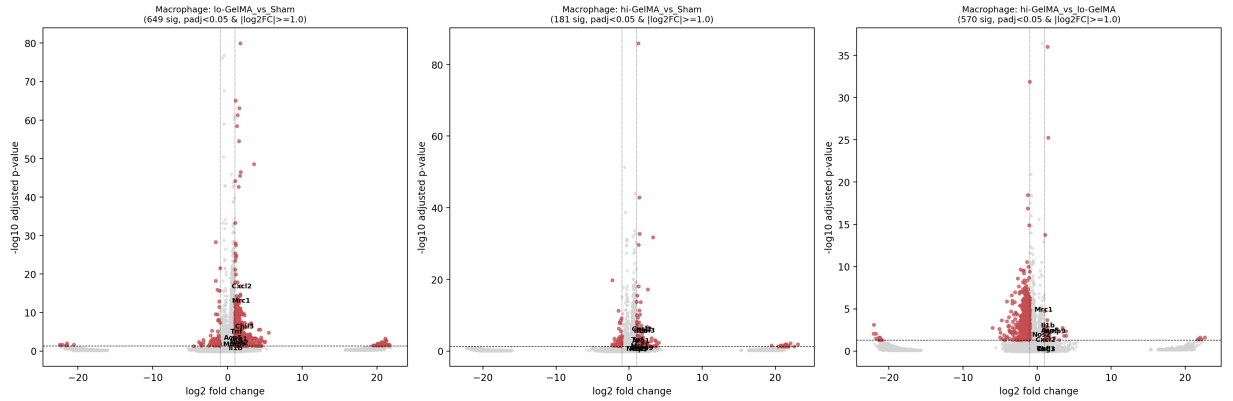

Figure 4. Macrophage differential expression for the three pairwise contrasts (Wilcoxon; $|\log_2 \mathrm{FC}| \geq 1$, $p_{\mathrm{adj}} < 0.05$). Counts of significant genes are annotated per panel. These cell-level tests are interpreted as effect-size rankings, not biological-replicate inference (Section 7).

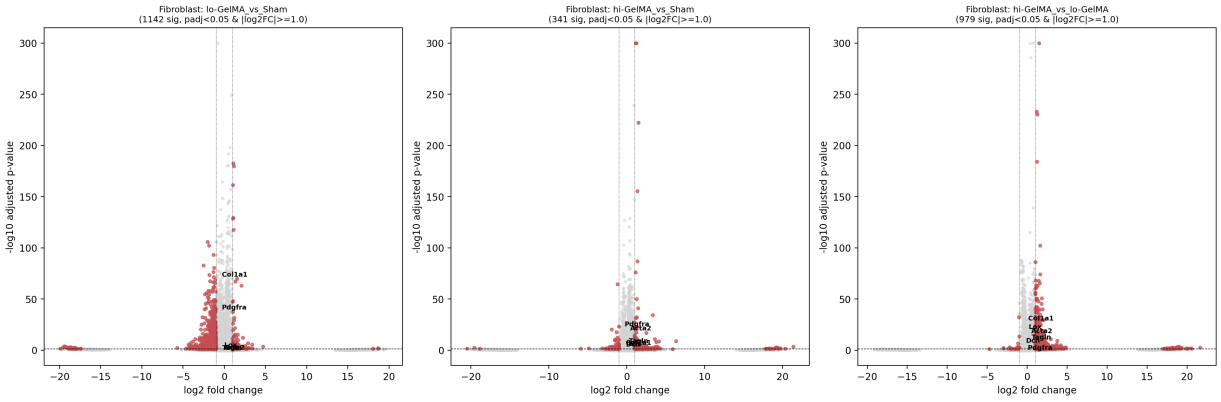

Figure 5. Fibroblast differential expression for the three pairwise contrasts. The hi-vs-lo contrast (right) is strongly skewed toward up-regulation (957 up vs 22 down), consistent with a broad activation shift under heavy crosslinking.

4.4 State versus composition: the inflammatory/fibrotic signal is a genuine cell-state shift

The decomposition (Figure 6; Table 2) is decisive for mechanism attribution. For *Il1b* in macrophages, the hi-vs-Sham and hi-vs-lo whole-tissue increases are classified as *predominantly state* changes—the within-cell transcriptional component (+0.478 and +0.409 $\log_2$FC) drives the signal, not a change in macrophage abundance. Likewise *Acta2* in fibroblasts is a *predominantly state* change in the hi-vs-Sham contrast, with the within-compartment component (+0.381) exceeding the whole-tissue value. In other words, heavy crosslinking makes individual macrophages more inflammatory and individual fibroblasts more contractile—it does not merely change how many of each cell there are. This is precisely the finding that a naive whole-tissue analysis would have blurred.

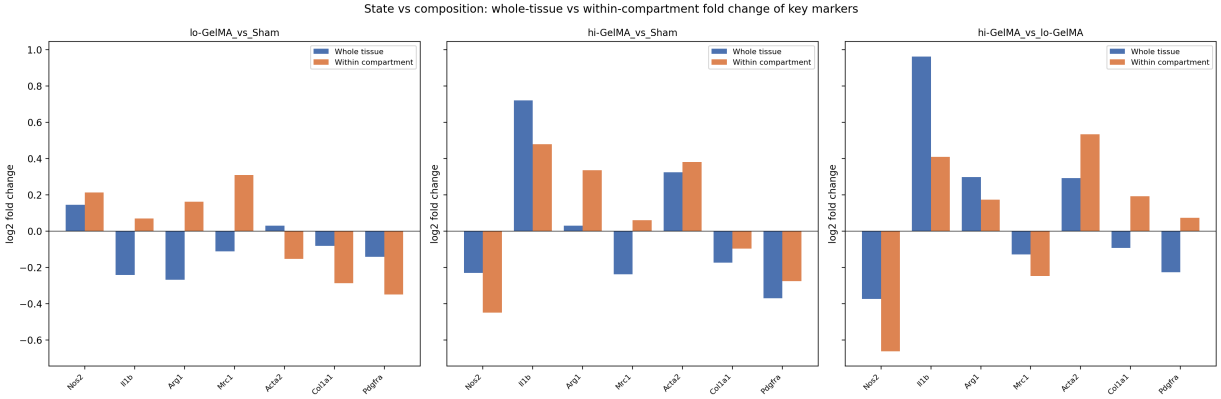

Figure 6. State versus composition decomposition. For each key marker and contrast, the observed whole-tissue $\log_2$ fold change (blue) is compared with the within-compartment (state) fold change (orange). Concordant, same-sign bars where the within-compartment component is large indicate genuine per-cell state changes (e.g. *Il1b* and *Acta2* under hi-GelMA), as opposed to composition-driven artefacts.

Table 2. Selected state-versus-composition results for the nominated mediators ($\log_2$ fold change). "State" = within-compartment; "Comp." = compartment-fraction.

Gene	Contrast	Whole	State	Comp.	Interpretation
Il1b	hi vs Sham	+0.721	+0.478	−0.310	predominantly state
Il1b	hi vs lo	+0.963	+0.409	+0.101	predominantly state
Acta2	hi vs Sham	+0.323	+0.381	−0.064	predominantly state
Acta2	hi vs lo	+0.293	+0.534	−0.280	(state; masked by comp.)
Nos2	hi vs lo	−0.375	−0.662	+0.101	predominantly state

4.5 Integrating material properties with cell states

Overlaying the four measured material properties on the eight single-cell readouts (Figures 7, 8) exposes the trade-off that drives the decision. The two gels are mechanically well separated: G' rises from ≈3 (lo-GelMA) to ≈150 (hi-GelMA, ∼50× stiffer), and the persistence area at PWD5 increases from 2.98 to 5.33 (hi-GelMA degrades more slowly). Yet phagocytic uptake collapses in the opposite direction: lo-GelMA is avidly taken up (pHrodo 7.33) whereas hi-GelMA is nearly inert to macrophage uptake (pHrodo 0.60), marking it as a persistent, poorly cleared foreign body. Descriptive correlations (reported strictly as n=3 effect-size rankings) are internally coherent: scaffold stiffness tracks the fibroblast contractile/migratory ratio (r=0.92); hydrogel uptake tracks fibroblast proportion (r=0.96) and inversely tracks the macrophage M1/M2 ratio ($r = -0.94$); and tissue infiltration tracks the fibroblast contractile/migratory ratio (r=0.97). A standardized PCA cleanly separates the three formulations, with PC1 (56.9%) and PC2 (43.1%) jointly explaining 100% of the variance—the mathematical ceiling for three samples, and itself a reminder of the design's limits.

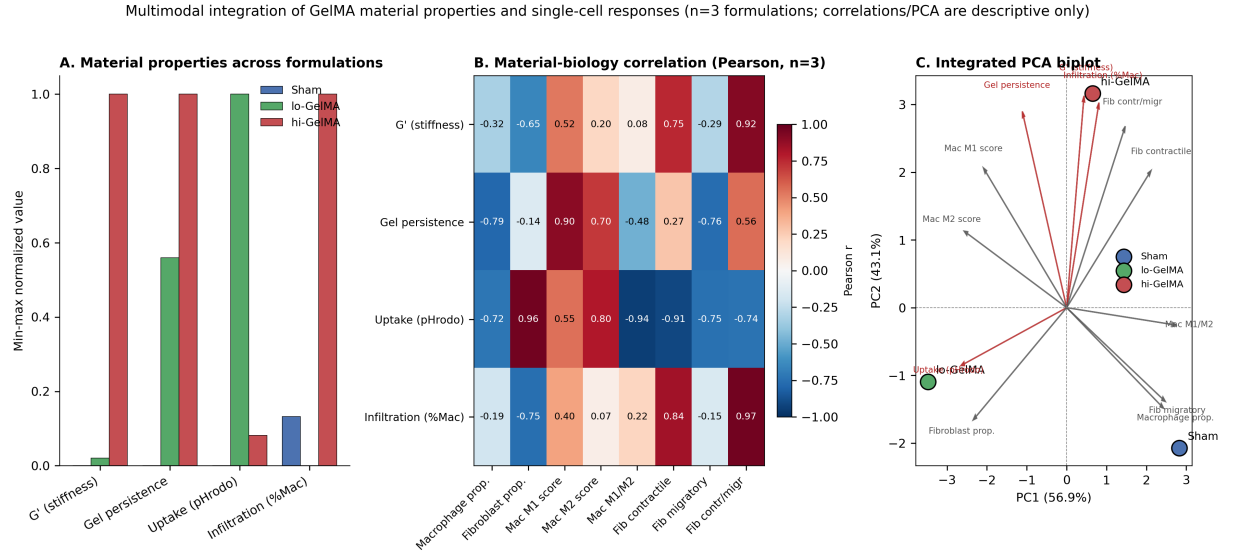

Figure 7. Material–biological integration. (A) Min–max normalised material properties across formulations. (B) Pearson correlation heatmap between the four material properties and eight cell-state readouts (n=3; descriptive only). (C) Standardized PCA biplot; the three formulations separate along PC1/PC2, with stiffness/persistence loadings opposing uptake and migratory-fibroblast loadings.

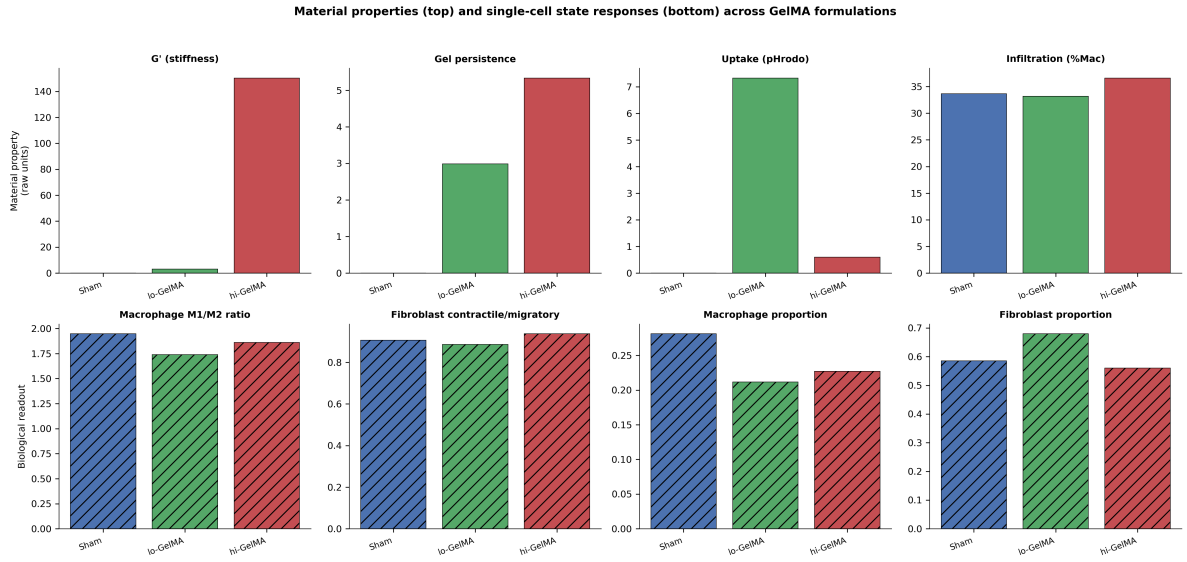

Figure 8. Material properties (top) and key cell-state metrics (bottom) across formulations. hi-GelMA is the stiffest and most persistent, yet is barely phagocytosed; it also carries the highest fibroblast contractile/migratory ratio. lo-GelMA inverts this profile. The intermediate design targets the favourable middle of each axis.

4.6 Robustness: the IL-1β/TNF-α $\rightarrow$ *Acta2*/*Col1a1* axis survives every stress test

Before nominating any mechanism, we required it to survive orthogonal sensitivity analyses. The cell-resampling bootstrap (Figure 9) shows the key contrasts are stable and non-zero: macrophage *Il1b* is up hi-vs-Sham (+0.478, 95% CI [0.240, 0.733]) and hi-vs-lo (+0.409, [0.199, 0.661]); macrophage *Tnf* is up in both gels versus Sham; fibroblast *Acta2* is up hi-vs-Sham (+0.381, [0.177, 0.519]) and hi-vs-lo (+0.534, [0.391, 0.684]); and *Col1a1* is up hi-vs-lo (+0.191, tight CI [0.163, 0.215]). Every one of these intervals excludes zero. The Leiden resolution sweep (Figure 10) shows every mediator contrast is sign-consistent across all five resolutions (e.g. *Il1b* hi-vs-Sham stays +0.477 to +0.499; *Acta2* hi-vs-lo stays +0.509 to +0.534), with compartment proportions stable at low/medium resolution and only mild drift at resolution ≥ 1.0. Independent sub-clustering (Figures 11, 12) localises the biology: the macrophage inflammatory increase under hi-GelMA is driven mainly by a per-cell state shift (higher *Il1b*/*Tnf* within cells) rather than expansion of a discrete M1 sub-cluster, whereas the fibroblast contractile activation reflects *both* an expanded contractile sub-population (Sham $\sim$0.34 $\rightarrow$ lo $\sim$0.46, hi $\sim$0.44) and elevated per-cell *Acta2*. The mechanism is thus robust in direction and significance and mechanistically coherent—meeting our pre-set bar for nomination.

4.7 The quantitative formulation decision matrix

Synthesising all of the above, we scored four formulations—Sham, lo-GelMA, hi-GelMA, and a proposed Intermediate GelMA—from 1 (least favourable) to 5 (most favourable) for regenerative wound healing across six material/biological dimensions (Table 3). Scores for the three tested arms are anchored on the measured Step 3–4 values; the Intermediate GelMA scores are *design targets*, explicitly aspirational rather than measured. The matrix yields a clear ranking: Intermediate GelMA (4.50) > lo-GelMA (3.17) > hi-GelMA (2.33) > Sham (1.83).

Quantitative anchors underlying the scores. G': Sham 0, lo $\approx$3, hi $\approx$150 (source-data relative

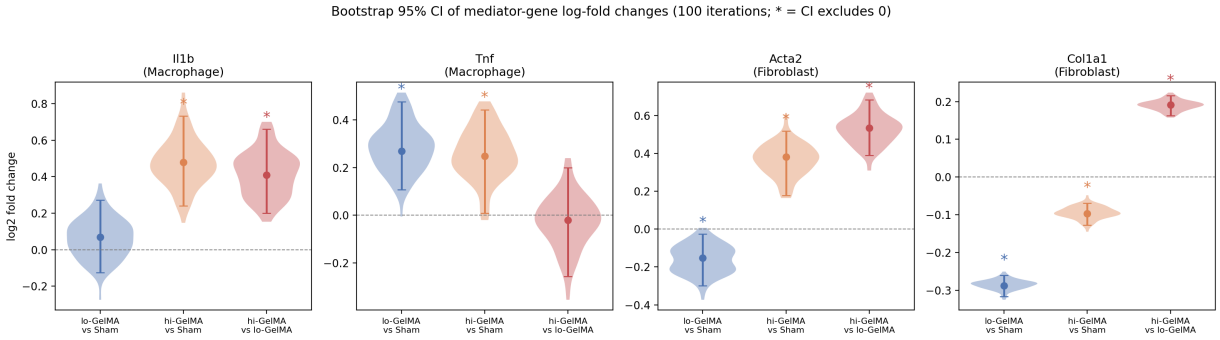

Figure 9. Cell-resampling bootstrap (100 iterations) of mediator-gene $\log_2$ fold changes. Violins show the bootstrap distribution; an asterisk marks contrasts whose 95% CI excludes zero. The macrophage *Il1b*/*Tnf* and fibroblast *Acta2*/*Col1a1* increases under heavy crosslinking are robust to cellular sampling.

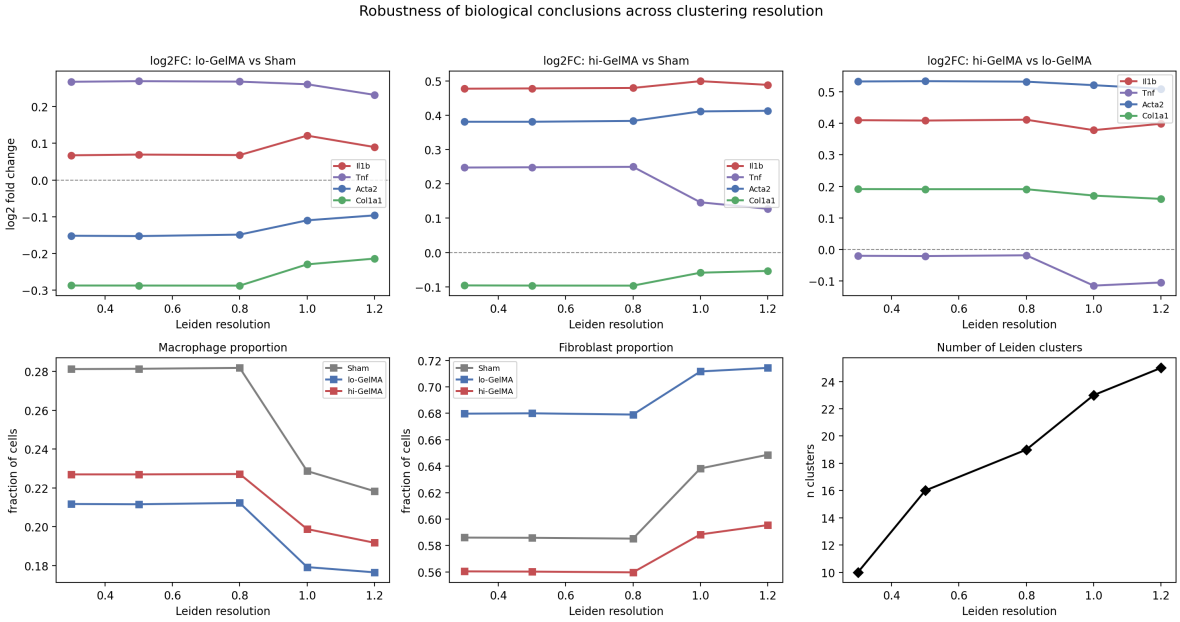

Figure 10. Clustering-resolution sensitivity. Mediator-gene $\log_2$FCs (top) and compartment proportions (bottom) recomputed across Leiden resolutions 0.3–1.2. Every mediator contrast is sign-consistent, confirming the biological conclusions do not depend on the resolution choice.

Table 3. Quantitative formulation decision matrix. Scores 1–5 (5 = most favourable for regenerative healing). The Intermediate GelMA row is scored on design targets, not measurements. Verbatim from `results/formulation_decision_matrix.csv`.

Formulation	**Mech.** G'	**Degrad.** persist.	**Uptake** phago.	**Infiltr.** depth	**Mac** M1/M2	**Fib** contr./migr.	**Total**	**Mean**	**Rank**
Sham	1	1	1	3	2	3	**11**	**1.83**	4
lo-GelMA	2	2	3	4	4	4	**19**	**3.17**	2
hi-GelMA	3	3	2	2	2	2	**14**	**2.33**	3
Interm. GelMA	5	5	4	5	4	4	**27**	**4.50**	**1**

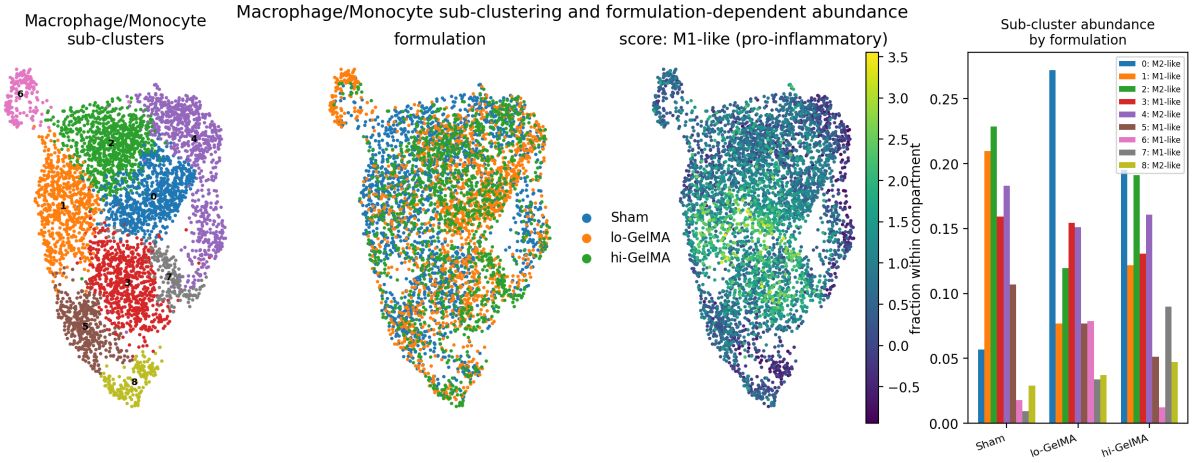

Figure 11. Macrophage sub-clustering on an independent embedding (9 sub-clusters). The hi-GelMA *Il1b*/*Tnf* increase is driven predominantly by a per-cell state shift rather than expansion of a discrete M1 sub-population.

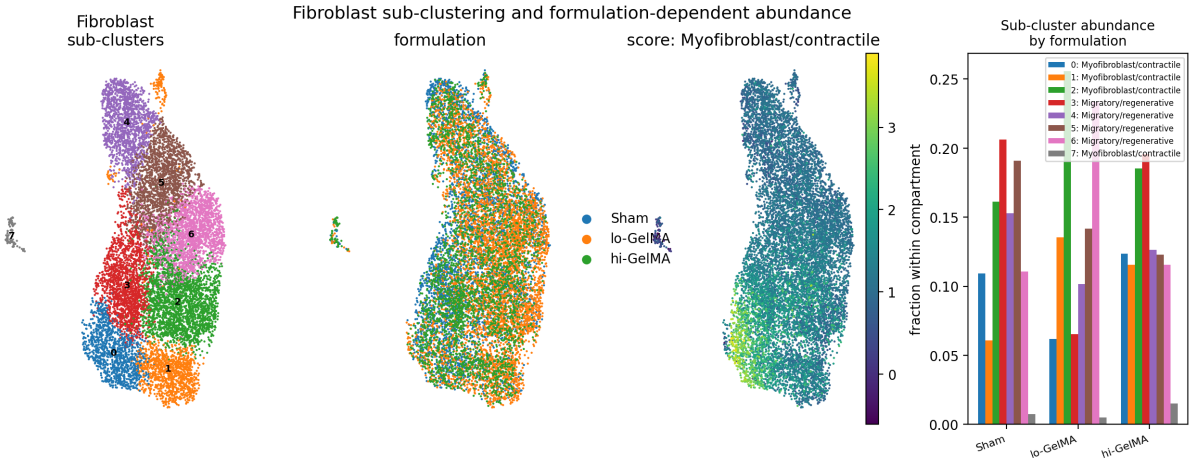

Figure 12. Fibroblast sub-clustering on an independent embedding (8 sub-clusters). The contractile/myofibroblast fraction expands from Sham to the GelMA groups, and per-cell *Acta2* is elevated—indicating both compositional and state contributions to contractile activation.

modulus; hi ∼50× stiffer; intermediate target 600–800 Pa). Degradation persistence area (PWD5): Sham 0, lo 2.98, hi 5.33 (intermediate target $t_{1/2}$∼14 d). pHrodo uptake: Sham 0, lo 7.33, hi 0.6. Macrophage recruitment: 33–37% across all groups (the discriminating variable being spatial *depth*, which single-cell data cannot resolve—this dimension is partly design-inferred). M1/M2 ratio: Sham 1.95, lo 1.74, hi 1.86. Fibroblast contractile/migratory ratio: Sham 0.906, lo 0.886, hi 0.938.

5 Discussion

5.1 Why an intermediate crosslink density, and not either tested gel

The decision matrix formalises a Goldilocks argument that each individual assay only hints at. The lightly crosslinked gel wins five of the six *biological* comparisons among the tested arms—it keeps macrophages closer to a pro-repair state, keeps fibroblasts migratory, and is efficiently cleared—but it fails the two *engineering* requirements a dressing must meet: at G'≈3 it provides essentially no load-bearing integrity, and it degrades before the proliferative phase is complete. Retaining it unchanged would trade a manageable biological problem for an unmanageable mechanical one. The heavily crosslinked gel is the mirror image: it is mechanically robust and persistent, but its density is mechanistically costly. It physically restricts infiltration; it resists phagocytic clearance (pHrodo 0.6), leaving a chronic foreign body; it expands neutrophils ($\log_2$ proportion FC +0.90 vs Sham); and—most importantly for the mechanism below—it pushes individual macrophages toward an IL-1β/TNF-α-high inflammatory state that couples to contractile myofibroblast activation and, by the original study's own account, to RANKL-driven macrophage fusion and pro-fibrotic remodelling [14]. Retaining hi-GelMA therefore locks in a pro-fibrotic trajectory. An intermediate crosslink density (G'∼600–800 Pa, $t_{1/2}$∼14 d) is the only option that can plausibly hold mechanical integrity through the proliferative phase while staying porous enough for ingress, clearable enough to avoid chronic foreign-body signalling, and soft enough to avoid the stiffness-driven myofibroblast program documented across the mechanobiology literature [9, 12, 13].

5.2 The nominated immune–stromal mechanism

We nominate a single axis for perturbation:

$$\text{Macrophage IL-1}\beta\text{/TNF-}\alpha \xrightarrow{\text{IL1R1, TNFRSF1A/1B}} \text{Fibroblast contractile activation } (\textit{Acta2},\ \textit{Col1a1}).$$

The nomination is disciplined, not opportunistic. Of the many candidate signals in the data, this axis is the one that (i) is a genuine per-cell *state* change, not a composition artefact (Table 2); (ii) has bootstrap 95% CIs excluding zero for the key mediators; and (iii) is sign-consistent across every clustering resolution tested. Its directionality is strongly supported by prior biology: macrophage-derived IL-1β and TNF-α are canonical inflammatory cytokines in wound repair and fibrosis, and macrophage–fibroblast crosstalk is an established engine of both productive repair and scar [2, 7, 11]. We note explicitly that the effect of IL-1β on fibroblasts is context-dependent in the literature—in some settings IL-1β can restrain myofibroblast formation—which is one more reason the axis must be *tested by perturbation* rather than assumed. The single-cell data can establish that these programs co-vary and suggest a direction; they cannot, on their own, prove that macrophage cytokine output causes fibroblast contraction.

5.3 Relationship to the source study and the broader literature

Our re-analysis is concordant with, and extends, the original report. Butenko et al. concluded that heavy crosslinking increases inflammation and pro-fibrotic fibroblast activity and identified a RANKL-mediated route to macrophage fusion [14]. We add three things useful for the next experiment: an explicit state-versus-composition decomposition that shows the inflammatory/fibrotic signal is transcriptional rather than compositional; a robustness audit that elevates the IL-1β/TNF-α axis specifically above other candidates as the safest single hypothesis; and a formulation-level integration that converts the biology into a concrete, quantitative design target rather than a binary soft-good/stiff-bad conclusion. The intermediate-crosslinking recommendation is consistent with the porous-implant and material-architecture literature, in which an optimised (neither minimal nor maximal) material presentation minimises fibrosis while supporting vascularised ingrowth [8, 10, 11].

6 Proposed Mechanistic Perturbation Experiment

Hypothesis. Inhibiting macrophage-derived IL-1β or TNF-α signalling within the intermediate hydrogel will reduce fibrotic myofibroblast activation (*Acta2*, *Col1a1*) and promote regenerative remodelling (*Pdgfra*, *Dcn*), without sacrificing the scaffold's mechanical integrity.

Exactly one target-specific perturbation is proposed, deliberately mirroring the discovery model to maximise interpretability while fixing its central weakness (replication).

Model. Female C57BL/6 full-thickness excisional skin wounds, silicone-splinted to minimise contraction and isolate the granulation/remodelling response [28], treated at the time of wounding with the intermediate GelMA (G'∼600–800 Pa).

Groups.

- **G1 — Intermediate GelMA + vehicle (PBS):** positive baseline for the inflammatory→fibrotic axis.
- **G2 — Intermediate GelMA + blockade:** the same gel co-delivering the IL-1 receptor antagonist **Anakinra** *or* the soluble TNF decoy **Etanercept** [29]. This is the target-specific arm.
- **G3 — Sham:** untreated wound, matching the original control.

Readouts and endpoints. Spatial transcriptomics maps whether blockade spatially decouples *Il1b*/*Tnf*-high macrophages from *Acta2*/*Col1a1*-high myofibroblasts at the gel–tissue interface—an interpretation grounded in ligand–receptor communication analysis [23, 24]. qPCR/ELISA quantify *Il1b*, *Tnf*, *Acta2*, *Col1a1* (fibrotic) and *Pdgfra*, *Dcn* (regenerative) transcripts plus IL-1β/TNF-α protein. Picrosirius-red polarised-light microscopy scores collagen maturation and scar architecture as the functional fibrosis endpoint [30]. Timepoints: days 7 and 14. **Primary endpoint:** reduced myofibroblast activation (*Acta2*/*Col1a1* transcript and protein) in G2 vs G1 at day 14. **Secondary:** increased regenerative markers, reduced/more-aligned collagen, and spatial dissociation of the macrophage–fibroblast inflammatory niche.

Power and design. $n \geq 5$–6 animals per group per timepoint, powered a priori. This biological replication directly remedies the discovery dataset's n=1 pooled-library confound and is what converts the axis from a robust association into a testable causal claim.

7 Statement of Causal Limitations

The formulation decision and nominated mechanism are *robust, reproducible effect-size rankings and directional hypotheses*—not population-level causal inferences. Three design constraints preclude causal claims from the discovery data alone.

1. n=3 **formulation-level constraint.** With a single value per formulation for each material property and aggregated biological readout, the correlations and PCA are restricted to *descriptive* effect-size rankings. Spearman ρ on three points can take only the values $\{-1, -0.5, 0, 0.5, 1\}$, and a PCA of three samples has at most two non-trivial components that trivially explain 100% of variance. No inferential statistic at the formulation level is possible.

2. n=1 **pooled-library batch confound.** Each formulation was profiled as a single pooled 10x library, so *formulation is completely confounded with sequencing batch.* Biological treatment effects cannot be separated from technical batch effects, and cell-level or pseudo-replicate p-values capture within-library technical variance rather than between-animal biological variance. Such p-values are anti-conservative and are used here only as effect-size rankings; batch "correction" is not attempted because it is mathematically inseparable from removing the treatment signal [19, 20, 25].

3. **Observational single-cell design.** Single-cell transcriptomics is a static, observational snapshot of co-occurring cell states. It can establish association and generate directional hypotheses (macrophage *Il1b*/*Tnf* co-varying with fibroblast *Acta2*/*Col1a1*) but cannot establish direct causality. The spatial *depth* of infiltration—one matrix dimension—likewise cannot be resolved from dissociated single-cell data and is partly design-inferred.

Mitigation. Every claim is reported at the appropriate epistemic level: measured material values and within-compartment effect sizes as robust, sensitivity-tested rankings; formulation-level correlations as descriptive only; and the immune–stromal mechanism as a hypothesis. The proposed in vivo perturbation with adequate biological replication (Section 7) is the designated route to causal confirmation, and the intermediate-gel target specifications (600–800 Pa, $t_{1/2}$∼14 d) are engineering hypotheses to be validated by direct rheological and degradation measurement before the biological arm begins.

8 Conclusion

Re-analysing the `GSE248524/PMC11315930` wound-scaffold dataset with a donor-aware, compartment-resolved, robustness-audited workflow resolves the central design question decisively: **neither tested gel should be advanced as-is**. The lightly crosslinked gel is biologically favourable but mechanically inadequate; the heavily crosslinked gel is mechanically adequate but biologically costly, driving a reproducible macrophage IL-1β/TNF-α $\rightarrow$ fibroblast *Acta2*/*Col1a1* program toward fibrosis. We recommend advancing an **Intermediate Crosslinked GelMA** (G'∼600–800 Pa, $t_{1/2}$∼14 d) that captures the structural virtues of hi-GelMA while restoring the bio-receptivity of

lo-GelMA, and we propose a single, target-specific IL-1/TNF-blockade experiment—powered with genuine biological replication—to convert the nominated mechanism from a robust association into a causal test. The strength of this recommendation lies not in any single number but in the convergence of independent material and cellular axes, and its honesty lies in the explicit boundary we draw around what an n=1, batch-confounded discovery dataset can prove.

Data and Reproducibility

Discovery data: GEO `GSE248524` and PMCID `PMC11315930` [14]. All analysis artefacts (annotated AnnData, differential and robustness summaries, the integrated material–biological matrix, and the decision matrix `results/formulation_decision_matrix.csv`) were generated with Scanpy 1.12.2 under a fixed seed (42) and are archived in the session directory. Every reference in this report was verified against the Crossref metadata API prior to inclusion; the research-lookup provenance is retained under `sources/`.

References

[1] Sabine A. Eming, Paul Martin, and Marjana Tomic-Canic. Wound repair and regeneration: Mechanisms, signaling, and translation. *Science Translational Medicine*, 6(265):265sr6, 2014. doi: 10.1126/scitranslmed.3009337.

[2] Thomas A. Wynn and Kevin M. Vannella. Macrophages in tissue repair, regeneration, and fibrosis. *Immunity*, 44(3):450–462, 2016. doi: 10.1016/j.immuni.2016.02.015.

[3] Boris Hinz. Formation and function of the myofibroblast during tissue repair. *The American Journal of Pathology*, 170(6):1807–1816, 2007. doi: 10.2353/ajpath.2007.070112.

[4] Yuval Rinkevich, Graham G. Walmsley, Michael S. Hu, Zeshaan N. Maan, Alexander M. Newman, Micha Drukker, Michael Januszyk, Geoffrey W. Krampitz, Geoffrey C. Gurtner, H. Peter Lorenz, Irving L. Weissman, and Michael T. Longaker. Identification and isolation of a dermal lineage with intrinsic fibrogenic potential. *Science*, 348(6232):aaa2151, 2015. doi: 10.1126/science.aaa2151.

[5] Shamik Mascharak, Heather E. desJardins Park, Michael F. Davitt, Michelle Griffin, Mimi R. Borrelli, Alessandra L. Moore, Kellen Chen, Bryan Duoto, Malini Chinta, Deshka S. Foster, Abra H. Shen, Michael Januszyk, Sun Hyung Kwon, Gerlinde Wernig, Derrick C. Wan, H. Peter Lorenz, Geoffrey C. Gurtner, and Michael T. Longaker. Preventing engrailed-1 activation in fibroblasts yields wound regeneration without scarring. *Science*, 372(6540):eaba2374, 2021. doi: 10.1126/science.aba2374.

[6] Matthew B. Buechler, Rachana N. Pradhan, Akshay T. Krishnamurty, Christian Cox, Aslihan K. Calviello, Amber W. Wang, Yeqing Angela Yang, Lucinda Tam, Roger Caothien, Merone Roose-Girma, Zora Modrusan, Joseph R. Arron, Richard Bourgon, Sören Muller, and Shannon J. Turley. Cross-tissue organization of the fibroblast lineage. *Nature*, 593(7860):575–579, 2021. doi: 10.1038/s41586-021-03549-5.

[7] Pardis Pakshir, Moien Alizadehgiashi, Brian Wong, Nuno M. Coelho, Xingyu Chen, Zhen Gong, Vivek B. Shenoy, Christopher A. McCulloch, and Boris Hinz. Dynamic fibroblast contractions attract remote macrophages in fibrillar collagen matrix. *Nature Communications*, 10:1850, 2019. doi: 10.1038/s41467-019-09709-6.

[8] James M. Anderson, Analiz Rodriguez, and David T. Chang. Foreign body reaction to biomaterials. *Seminars in Immunology*, 20(2):86–100, 2008. doi: 10.1016/j.smim.2007.11.004.

[9] Kan Yue, Grissel Trujillo-de Santiago, Mario Moises Alvarez, Ali Tamayol, Nasim Annabi, and Ali Khademhosseini. Synthesis, properties, and biomedical applications of gelatin methacryloyl (GelMA) hydrogels. *Biomaterials*, 73:254–271, 2015. doi: 10.1016/j.biomaterials.2015.08.045.

[10] Eric M. Sussman, Michelle C. Halpin, Jeanot Muster, Randall T. Moon, and Buddy D. Ratner. Porous implants modulate healing and induce shifts in local macrophage polarization in the foreign body reaction. *Annals of Biomedical Engineering*, 42(7):1508–1516, 2014. doi: 10.1007/s10439-013-0933-0.

[11] Karen E. Martin and Andrés J. García. Macrophage phenotypes in tissue repair and the foreign body response: Implications for biomaterial-based regenerative medicine strategies. *Acta Biomaterialia*, 133: 4–16, 2021. doi: 10.1016/j.actbio.2021.03.038.

[12] Xiaojuan Huang, Ning Yang, Victor F. Fiore, Thomas H. Barker, Yong Sun, Samuel W. Morris, Qiang Ding, Victor J. Thannickal, and Yong Zhou. Matrix stiffness-induced myofibroblast differentiation is mediated by intrinsic mechanotransduction. *American Journal of Respiratory Cell and Molecular Biology*, 47(3):340–348, 2012. doi: 10.1165/rcmb.2012-0050OC.

[13] Alba Santos and David Lagares. Matrix stiffness: The conductor of organ fibrosis. *Current Rheumatology Reports*, 20(1):2, 2018. doi: 10.1007/s11926-018-0710-z.

[14] Sergei Butenko, Raji R. Nagalla, Christian F. Guerrero-Juarez, Francesco Palomba, Li-Mor David, Ronald Q. Nguyen, Denise Gay, Axel A. Almet, Michelle A. Digman, Qing Nie, Philip O. Scumpia, Maksim V. Plikus, and Wendy F. Liu. Hydrogel crosslinking modulates macrophages, fibroblasts, and their communication, during wound healing. *Nature Communications*, 15(1):6820, 2024. doi: 10.1038/s41467-024-50072-y.

[15] Grace X. Y. Zheng, Jessica M. Terry, Phillip Belgrader, Paul Ryvkin, Zachary W. Bent, Ryan Wilson, Solongo B. Ziraldo, Tobias D. Wheeler, Geoff P. McDermott, Junjie Zhu, et al. Massively parallel digital transcriptional profiling of single cells. *Nature Communications*, 8:14049, 2017. doi: 10.1038/ncomms14049.

[16] F. Alexander Wolf, Philipp Angerer, and Fabian J. Theis. SCANPY: Large-scale single-cell gene expression data analysis. *Genome Biology*, 19:15, 2018. doi: 10.1186/s13059-017-1382-0.

[17] Samuel L. Wolock, Romain Lopez, and Allon M. Klein. Scrublet: Computational identification of cell doublets in single-cell transcriptomic data. *Cell Systems*, 8(4):281–291.e9, 2019. doi: 10.1016/j.cels.2018.11.005.

[18] V. A. Traag, L. Waltman, and N. J. van Eck. From louvain to leiden: Guaranteeing well-connected communities. *Scientific Reports*, 9:5233, 2019. doi: 10.1038/s41598-019-41695-z.

[19] Jordan W. Squair, Matthieu Gautier, Claudia Kathe, Mark A. Anderson, Nicholas D. James, Thomas H. Hutson, Rémi Hudelle, Taha Qaiser, Kaya J. E. Matson, Quentin Barraud, Ariel J. Levine, Gioele La Manno, Michael A. Skinnider, and Grégoire Courtine. Confronting false discoveries in single-cell differential expression. *Nature Communications*, 12:5692, 2021. doi: 10.1038/s41467-021-25960-2.

[20] Alan E. Murphy and Nathan G. Skene. A balanced measure shows superior performance of pseudobulk methods in single-cell rna-sequencing analysis. *Nature Communications*, 13:7851, 2022. doi: 10.1038/s41467-022-35519-4.

[21] Helena L. Crowell, Charlotte Soneson, Pierre-Luc Germain, Daniela Calini, Ludovic Collin, Catarina Raposo, Dheeraj Malhotra, and Mark D. Robinson. muscat detects subpopulation-specific state transitions from multi-sample multi-condition single-cell transcriptomics data. *Nature Communications*, 11: 6077, 2020. doi: 10.1038/s41467-020-19894-4.

[22] Emma Dann, Neil C. Henderson, Sarah A. Teichmann, Michael D. Morgan, and John C. Marioni. Differential abundance testing on single-cell data using k-nearest neighbor graphs. *Nature Biotechnology*, 40(2):245–253, 2022. doi: 10.1038/s41587-021-01033-z.

[23] Suoqin Jin, Christian F. Guerrero-Juarez, Lihua Zhang, Ivan Chang, Raul Ramos, Chen-Hsiang Kuan, Peggy Myung, Maksim V. Plikus, and Qing Nie. Inference and analysis of cell-cell communication using cellchat. *Nature Communications*, 12:1088, 2021. doi: 10.1038/s41467-021-21246-9.

[24] Suoqin Jin, Maksim V. Plikus, and Qing Nie. Cellchat for systematic analysis of cell-cell communication from single-cell transcriptomics. *Nature Protocols*, 20:180–219, 2024. doi: 10.1038/s41596-024-01045-4.

[25] Laleh Haghverdi, Aaron T. L. Lun, Michael D. Morgan, and John C. Marioni. Batch effects in single-cell RNA-sequencing data are corrected by matching mutual nearest neighbors. *Nature Biotechnology*, 36 (5):421–427, 2018. doi: 10.1038/nbt.4091.

[26] Malte D. Luecken, M. Büttner, K. Chaichoompu, A. Danese, M. Interlandi, M. F. Müller, D. C. Strobl, L. Zappia, M. Dugas, M. Colomé-Tatché, and Fabian J. Theis. Benchmarking atlas-level data integration in single-cell genomics. *Nature Methods*, 19(1):41–50, 2022. doi: 10.1038/s41592-021-01336-8.

[27] Aaron T. L. Lun, Davis J. McCarthy, and John C. Marioni. A step-by-step workflow for low-level analysis of single-cell RNA-seq data with bioconductor. *F1000Research*, 5:2122, 2016. doi: 10.12688/f1000research.9501.2.

[28] Robert D. Galiano, Joseph Michaels, Michael Dobryansky, Jamie P. Levine, and Geoffrey C. Gurtner. Quantitative and reproducible murine model of excisional wound healing. *Wound Repair and Regeneration*, 12(4):485–492, 2004. doi: 10.1111/j.1067-1927.2004.12404.x.

[29] David Dixon, Jonathon Coates, Alicia del Carpio Pons, Joanna Horabin, Andrew Walker, Nicole Abdul, Nicholas S. Kalson, Nigel T. Brewster, David J. Weir, David J. Deehan, Derek A. Mann, and Lee A. Borthwick. A potential mode of action for anakinra in patients with arthrofibrosis following total knee arthroplasty. *Scientific Reports*, 5:16466, 2015. doi: 10.1038/srep16466.

[30] L. C. U. Junqueira, G. Bignolas, and R. R. Brentani. Picrosirius staining plus polarization microscopy, a specific method for collagen detection in tissue sections. *The Histochemical Journal*, 11(4):447–455, 1979. doi: 10.1007/BF01002772.